

Intrinsic $1T'$ phase induced in atomically thin $2H$ - MoTe_2 by a single terahertz pulse

Received: 15 October 2022

Accepted: 29 August 2023

Published online: 22 September 2023

Check for updates

Jiaojian Shi ^{1,15}, Ya-Qing Bie ^{2,3,15} ✉, Alfred Zong ^{2,4,15}, Shiang Fang ^{5,6,14}, Wei Chen ⁵, Jinchi Han ^{7,8}, Zhaolong Cao³, Yong Zhang⁹, Takashi Taniguchi ¹⁰, Kenji Watanabe ¹¹, Xuewen Fu ¹², Vladimir Bulović ⁷, Efthimios Kaxiras ⁵, Edoardo Baldini ¹³, Pablo Jarillo-Herrero ² ✉ & Keith A. Nelson ¹ ✉

The polymorphic transition from $2H$ to $1T'$ - MoTe_2 , which was thought to be induced by high-energy photon irradiation among many other means, has been intensely studied for its technological relevance in nanoscale transistors due to the remarkable improvement in electrical performance. However, it remains controversial whether a crystalline $1T'$ phase is produced because optical signatures of this putative transition are found to be associated with the formation of tellurium clusters instead. Here we demonstrate the creation of an intrinsic $1T'$ lattice after irradiating a mono- or few-layer $2H$ - MoTe_2 with a single field-enhanced terahertz pulse. Unlike optical pulses, the low terahertz photon energy limits possible structural damages. We further develop a single-shot terahertz-pump-second-harmonic-probe technique and reveal a transition out of the $2H$ -phase within 10 ns after photoexcitation. Our results not only provide important insights to resolve the long-standing debate over the light-induced polymorphic transition in MoTe_2 but also highlight the unique capability of strong-field terahertz pulses in manipulating quantum materials.

Tailored, ultrashort pulses of light can be used to manipulate metastable states¹ in functional materials, such as triggering insulator-to-metal transitions², unveiling hidden states³, or even inducing long-lasting superconducting-like behavior way above the equilibrium critical temperature⁴. These photoinduced states have been intensely

studied not only because they yield profound insights into fundamental light-matter interactions in correlated systems but also because they bring new opportunities to the field of laser fabrication and micro-machining, going beyond traditional laser cutting⁵, burning⁶, or stereolithography technologies⁷. From this application

¹Department of Chemistry, Massachusetts Institute of Technology, Cambridge, MA 02139, USA. ²Department of Physics, Massachusetts Institute of Technology, Cambridge, MA 02139, USA. ³State Key Lab of Optoelectronic Materials and Technologies, Guangdong Province Key Laboratory of Display Material and Technology, School of Electronics and Information Technology, Sun Yat-sen University, Guangzhou 510275, People's Republic of China. ⁴Department of Chemistry, University of California, Berkeley, CA 94720, USA. ⁵Department of Physics, Harvard University, Cambridge, MA 02138, USA. ⁶Department of Physics and Astronomy, Center for Materials Theory, Rutgers University, Piscataway, NJ 08854, USA. ⁷Department of Electrical Engineering and Computer Science, Massachusetts Institute of Technology, Cambridge, MA 02139, USA. ⁸School of Integrated Circuits, Peking University, Beijing 100871, People's Republic of China. ⁹Center for Materials Science & Engineering, Massachusetts Institute of Technology, Cambridge, MA 02139, USA. ¹⁰International Center for Materials Nanoarchitectonics, National Institute for Materials Science, 1-1 Namiki, Tsukuba 305-0044, Japan. ¹¹Research Center for Functional Materials, National Institute for Materials Science, 1-1 Namiki, Tsukuba 305-0044, Japan. ¹²Ultrafast Electron Microscopy Laboratory, The MOE Key Laboratory of Weak-Light Nonlinear Photonics, School of Physics, Nankai University, Tianjin 300071, People's Republic of China. ¹³Department of Physics, Center for Complex Quantum System, The University of Texas at Austin, Austin, TX 78712, USA. ¹⁴Present address: Department of Physics, Massachusetts Institute of Technology, Cambridge, MA 02139, USA. ¹⁵These authors contributed equally: Jiaojian Shi, Ya-Qing Bie and Alfred Zong. ✉ e-mail: bieyq@mail.sysu.edu.cn; pjarillo@mit.edu; kanelson@mit.edu

perspective, the metastable $17'$ phase of MoTe_2 induced in a semi-conducting $2H$ polymorph is considered an important candidate for tackling the issue of high contact resistance for two-dimensional electrical device⁸. In this polymorphic transition, the hexagonal unit cell of $2H\text{-MoTe}_2$ in its ground state is transformed into the metastable $17'$ phase after going through an intermediate structure (Fig. 1a), a process that was believed to be readily instigated by optical irradiation^{9–13}. Compared to other methods^{14,15} such as ionic gating^{16,17} and strain application¹⁸, the focused laser spot down to the sub-micrometer regime makes an optically driven transition especially appealing for precision fabrication of small devices.

Despite the high technological impact of this polymorphic transition in MoTe_2 , recent studies have cast doubt on the existence of the purported $17'$ structure upon optical illumination. In particular, the main evidence for the $17'$ polymorph was the A_g phonon peaks around 120 cm^{-1} and 140 cm^{-1} in Raman spectroscopy^{19,20} (Supplementary Figs. 1 and 2), which have been shown to originate from nano- or micro-sized Te clusters. Given the high energy barrier E_{barrier} of more than 0.8 eV per MoTe_2 formula unit²¹ as well as the large Te displacement of more than 1 \AA required for the transition²² (Fig. 1a), it remains unclear whether light can initiate the polymorphic change after all.

In this work, instead of using visible light, we report the successful transition from $2H$ to $17'\text{-MoTe}_2$ using single-cycle, field-enhanced terahertz (THz) pulses. The transition can be induced with as few as a single THz pulse on atomically thin crystals of $2H\text{-MoTe}_2$. Using Raman spectroscopy, we show that the induced phase reflects an intrinsic $17'$ structure^{16,17,23}, which is free from any spurious features associated with Te clusters. The validity of the metastable $17'$ phase is further confirmed by selected area electron diffraction and energy-dispersive

X-ray spectroscopy, which demonstrate a macroscopic structural transition without stoichiometric changes in the sample. Using single-shot, time-resolved nonlinear optical spectroscopy, we also unveil the different stages of this irreversible phase transition. These findings provide a route of structural manipulation using high-field THz pulses, which crucially avoid large-scale defect generation that often accompanies intense optical excitation⁹.

Results

Polymorphic transition in monolayer MoTe_2

In our experiments, we positioned a flake of $2H\text{-MoTe}_2$ encapsulated by hexagonal-boron nitride (h-BN) on top of two parallel gold strips separated by a gap (Fig. 1b). The h-BN layers were used to isolate monolayers and bilayer MoTe_2 samples from field-induced emission in the gold layers²⁴ and to prevent their direct exposure to air. Figure 1d shows the optical image of a monolayer sample prepared using a dry transfer method²⁵. Upon illumination of this structure with a free-space THz pulse, the field strength can be enhanced by more than 100 times at certain hot spots and about 20 times at the gap center, as shown in Fig. 1c. Since the peak electric field of the THz pulse in free space reached $\sim 300\text{ kV/cm}$ at the focus, the electrical field amplitude can be more than 5 MV/cm in large parts of the sample²⁶ (see Fig. 1c, Supplementary Fig. 3, “Methods” section, and Supplementary Note 1 for detailed information on THz generation). After irradiating this structure with a free-space THz field of 270 kV/cm , we probed lattice changes via spontaneous Raman scattering. Figure 1e shows the Raman spectra. Before the THz illumination, the spectrum consists of the A_{1g} phonon at 171.5 cm^{-1} and the E_{2g} phonon at 236 cm^{-1} , in agreement with previous studies of the $2H$ phase²². After excitation

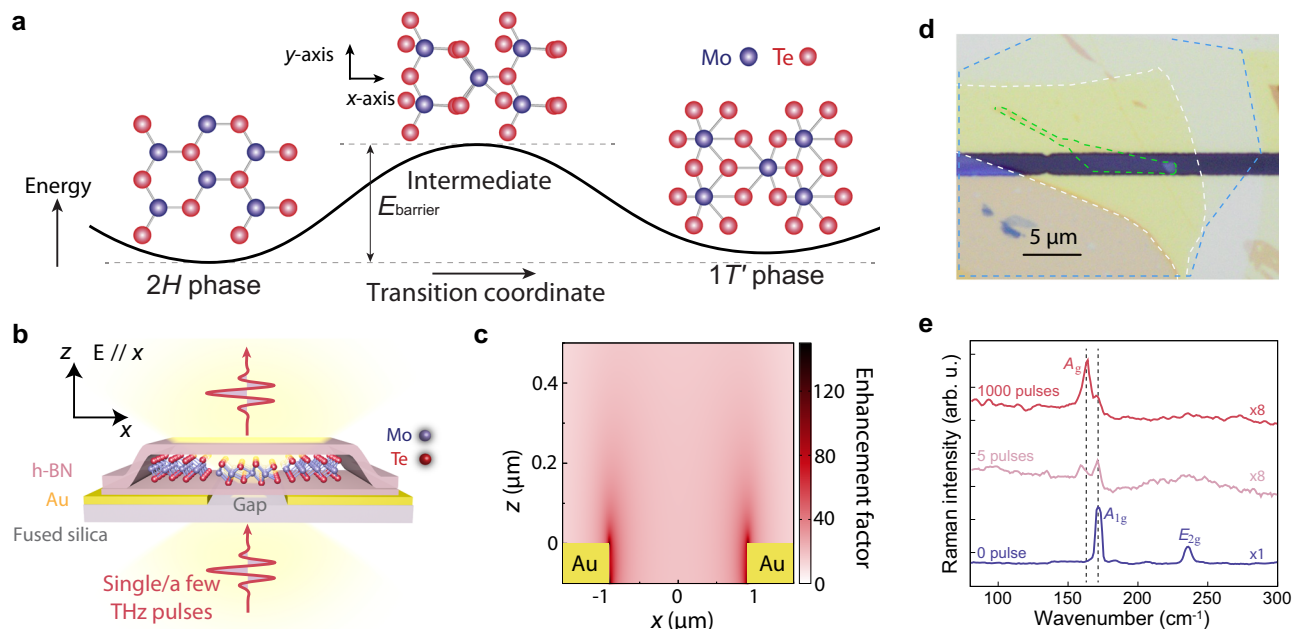


Fig. 1 | Polymorphic transition in MoTe_2 induced by high-field THz pulses.

a Schematic energy landscape and top view of lattice structures of $2H\text{-MoTe}_2$ (left), the intermediate state (middle), and $17'\text{-MoTe}_2$ (right). E_{barrier} is the potential barrier between the $2H$ and $17'$ -phase. **b** Cross-sectional schematic illustration of a $2H\text{-MoTe}_2$ crystal spanning an insulating gap between deposited gold strips, which serve as a THz field enhancement structure. The monolayer $2H\text{-MoTe}_2$ crystal is encapsulated between top and bottom h-BN. THz pulses are incident from the bottom side of the fused silica substrate. **c** Field strength calculation of the THz enhancement structure. Numerical simulation results showing THz field enhancement by a factor of 20–50 in significant regions in and near the gap between the gold strips. The enhancement factor is defined as the ratio between the actual and incident electric field. **d** Optical micrograph of a monolayer sample, including a 15-

nm-thick top h-BN (white dashed line), a monolayer $2H\text{-MoTe}_2$ (green dashed line), and a 5-nm-thick bottom h-BN (blue dashed line), all spanning a $1.8\text{-}\mu\text{m}$ insulating gap (dark horizontal line) between the top and bottom gold strips. **e** Raman spectra of monolayer MoTe_2 after successive THz pulse irradiation with free-space field amplitudes of 270 kV/cm . The A_g mode of the $17'$ phase sets in after 5 THz pulses and dominates upon further irradiation. By contrast, the A_{1g} and E_{2g} modes of the $2H$ phase are strongly reduced. The reduction of the overall Raman intensity in monolayer samples may be related to compromised crystallinity after the irradiation. The Raman measurements were conducted with a $1\text{-}\mu\text{m}$ -diameter laser spot and were therefore averaged over regions that had been subjected to differently enhanced THz field strengths. The two dashed lines are aligned with the A_g and A_{1g} mode of the $17'$ and $2H$ -phase, respectively.

with five THz pulses, both modes of the $2H$ phase disappear and a peak at 163.3 cm^{-1} emerges (see Supplementary Fig. 4 for additional peak width analysis). This feature signifies a change of the crystalline symmetry, and it is considered a specific fingerprint of the $17'$ phase of MoTe_2 ^{16,22}. The new phonon peak becomes more prominent after further exposure to THz pulses (Fig. 1e), indicating the growth of a larger $17'$ sample area. Importantly, the spectrum does not show any localized modes due to damage-related Te clusters¹⁹ even though the resultant $17'$ phase is not homogeneously produced in the flake suspended between the gap of the gold strips (Supplementary Figs. 5 and 6). These observations were reproduced in multiple samples, suggesting that the action of a strong THz field on our monolayer MoTe_2 is to induce a phase transition from the $2H$ to the $17'$ polymorph.

To further investigate this structural transformation, we conducted experiments on a series of monolayer $2H\text{-MoTe}_2$ samples. Since the induced $17'$ phase is long-lived, each measurement required a fresh specimen that was carefully positioned over the gap between the gold strips, as indicated in Fig. 1b. First, we studied how the $2H$ phase responded to a sequence of THz pulses with a gradually increasing field strength. To probe the phase transition, we tracked the changes in crystalline symmetry via optical second harmonic generation (SHG), a sensitive probe of inversion symmetry breaking that can distinguish

between the non-centrosymmetric $2H$ phase and the centrosymmetric $17'$ phase in samples with an odd number of layers^{27,28} (see “Methods” section). Figure 2a shows three representative real-space images of the SHG intensity before and after THz-field exposures with free-space amplitudes of 210 kV/cm and 240 kV/cm; additional SHG intensity images are shown in Supplementary Fig. 7. A plot of the SHG intensities from three sample locations within the field-enhancement gap (labeled I, II, III in Fig. 2a) is presented in Fig. 2b. We observe that the SHG signal drops when the field strength exceeds 183 kV/cm, disappearing completely above 270 kV/cm. As the field enhancement factor generated by the gold strips is around 20, the threshold needed to quench the SHG intensity is estimated to be approximately 4.0 MV/cm. We complemented these measurements by recording Raman spectra as a function of the THz field strength. Figure 2c shows the spectra acquired after irradiation at 200 kV/cm and 270 kV/cm. Consistent with the picture supported by the SHG results in Fig. 2b, a single-pulse irradiation first leads to a drop in the intensity of the $2H$ phonons with a free-space field strength of 200 kV/cm, and stronger THz pulses at 270 kV/cm subsequently cause a further suppression, leading to a nearly complete extinction of the peak after 1000 pulses. Simultaneously, the Raman mode of the $17'$ phase grows, eventually dominating the spectrum.

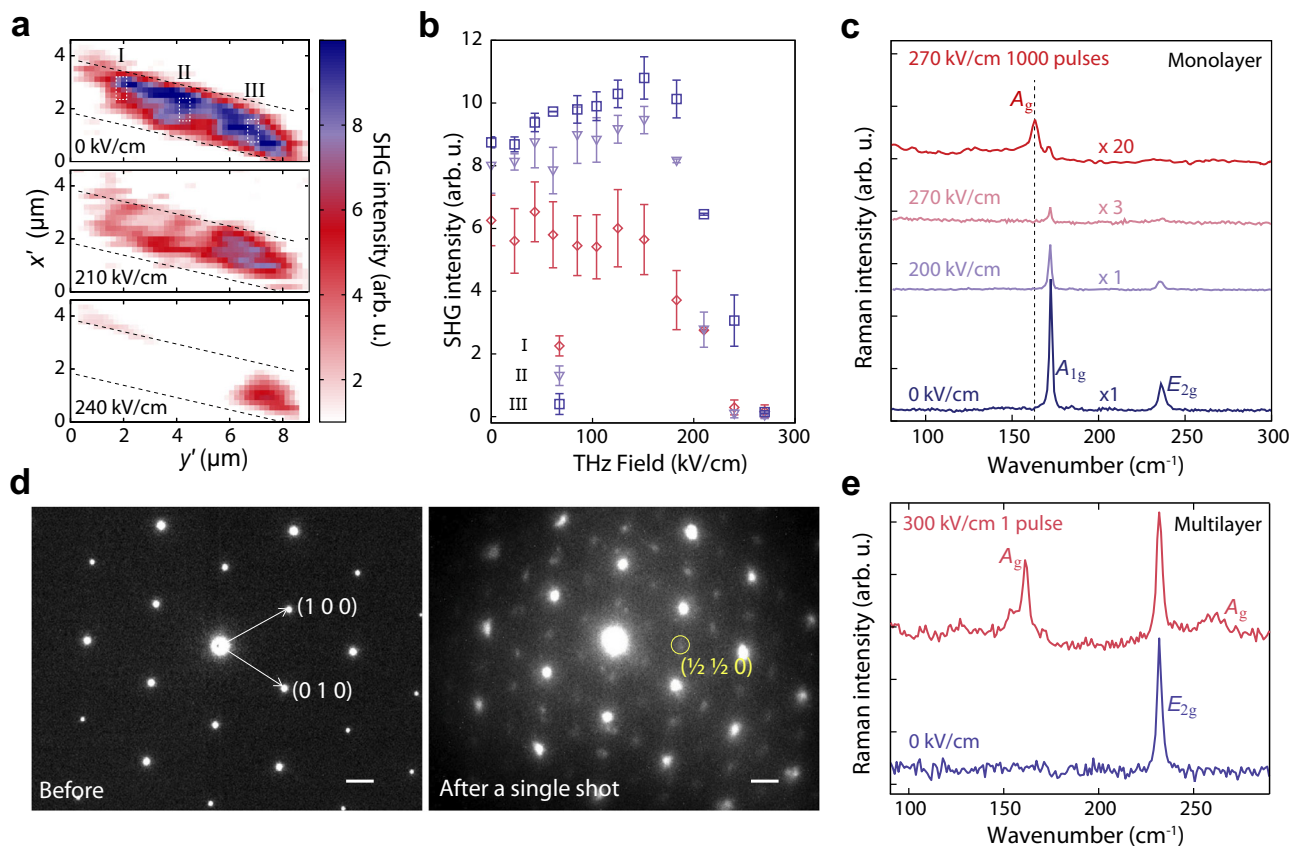


Fig. 2 | THz field dependence of the phase transition in monolayer and multilayer MoTe_2 . **a** SHG images of monolayer MoTe_2 before THz irradiation (0 kV/cm), after irradiation with one THz pulse at 210 kV/cm free-space field amplitude, and after irradiation with a second THz pulse at 240 kV/cm. The dashed lines indicate the edges of gold strips in the field enhancement structure. Different areas of monolayer MoTe_2 in the gap are outlined by the white dashed boxes and labeled by I, II, and III. The primes in x' and y' of the axes are added to differentiate the x - y coordinates in Fig. 1 due to the rotated field of view in SHG microscopy. **b** SHG from different areas (I–III) in **a** measured after irradiation of the sample by single THz pulses with successively increasing field strength. The vertical error bars measure the deviation of the averaged SHG intensity in the regions of interest from that of

nearby pixels in the image. **c** Raman spectra of monolayer MoTe_2 samples prior to THz irradiation (blue curve), after THz irradiation with a single pulse at 200 kV/cm (violet curve), another single pulse at 270 kV/cm (pink curve), and 1000 pulses at 270 kV/cm (red curve). The monolayer MoTe_2 sample shows the A_g mode at 163.5 cm^{-1} after irradiation with 1000 pulses at 270 kV/cm. **d** Electron diffraction pattern of a multilayer (~ 10 layers) MoTe_2 before and after a single THz pulse irradiation at 300 kV/cm, showing the emergence of superstructure peaks (yellow circle) that are characteristic of the $17'$ phase. The scale bars represent 0.1 \AA^{-1} . **e** Raman spectra of the multilayer MoTe_2 before and after a single THz pulse irradiation at 300 kV/cm, showing the emergence of new Raman peaks that are characteristic of the induced $17'$ phase.

Polymorphic transition in multilayer MoTe₂

The THz-induced transition is not restricted to monolayer samples, and we observed similar phenomenology in bilayer and multilayer (-10 layers) 2H-MoTe₂ (see Supplementary Figs. 6c, d and 8a, b). Figure 2d, e show the results obtained on a multilayer 2H-MoTe₂, presenting the [001] zone-axis electron diffraction pattern and Raman spectra before and after irradiation with a single THz pulse at 300 kV/cm. We find that the diffraction pattern of the unexcited crystal exhibits the six-fold symmetry expected for the 2H phase. Consistent with this observation, the Raman spectrum only displays an E_{2g} phonon mode of bulk 2H-MoTe₂²⁹. After THz irradiation, new peaks emerge in the diffraction pattern taken along the [001] zone axis of the new unit cell (Fig. 2d), revealing a cell-doubling superstructure^{30–33}. On the other hand, our energy-dispersive X-ray spectroscopy mapping of the irradiated sample shows that the stoichiometric ratio of -1:2 is maintained and Te clusters are absent (Supplementary Fig. 9). The change in the electron diffraction pattern is accompanied by the appearance of A_g phonons (164 cm⁻¹ and 270 cm⁻¹) in the Raman spectrum (Fig. 2e)^{16,19}. Both observables are characteristic signatures of the 1T' lattice, offering additional validation for the creation of an intrinsic 1T' phase (see Supplementary Note 2 and 3, and Supplementary Fig. 10).

Temporal evolution of the polymorphic transition

To gain microscopic insights into the THz-driven transition, we also examined the photo-induced dynamics to trace out the temporal evolution of the crystalline lattice. This investigation cannot be accomplished by conventional time-resolved spectroscopy methods because their stroboscopic approach precludes the study of irreversible processes. We therefore developed a specialized apparatus for THz pump-SHG probe single-shot spectroscopy, which is well suited for probing the formation dynamics of the long-lived metastable 1T' state. A schematic illustration of our experiment is presented in Fig. 3a; details of the setup are described in Methods. In our measurements, we irradiated trilayer samples with a single THz pulse, whose field strength was adjusted to exceed the phase transition threshold. We subsequently recorded the SHG signal at different pump-probe delays. Since the THz field was above the threshold for generating the 1T' phase, the experiment was challenging because each THz shot with its predetermined delay time needed to be conducted on a fresh piece of sample. An added difficulty is the extremely weak single-shot SHG signal from a few-layer sample; using a photomultiplier tube, we obtained measurable second harmonic intensity under an incident 800-nm pulse fluence of ~20 mJ/cm², which is beyond the optical damage threshold. Here, the collection of single-shot SHG signals

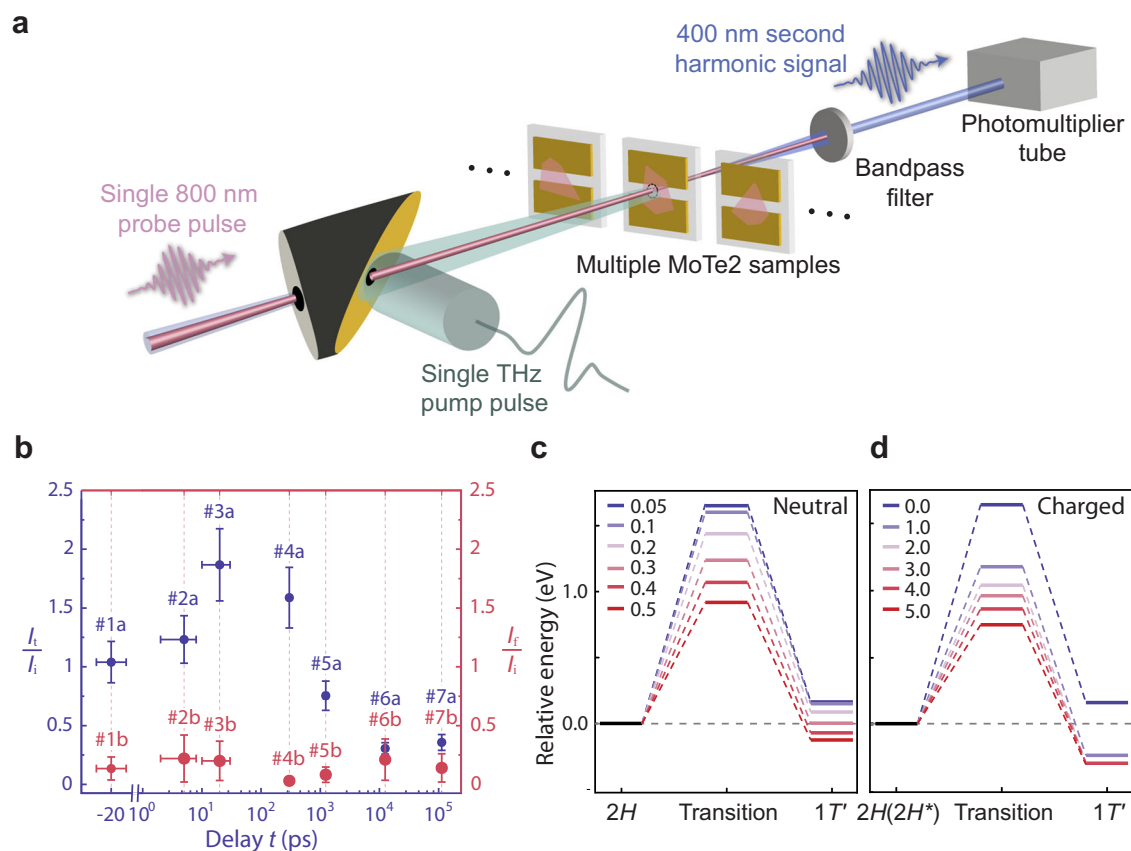


Fig. 3 | Dynamics and driving mechanism of the THz-field-induced phase transition. **a** Schematic illustration of the setup for single-shot SHG probe with a THz excitation pulse. Single-shot measurements were conducted by using a fresh sample in each shot. **b** SHG intensities measured from trilayer MoTe₂ samples at different delay times t from several picoseconds to hundreds of nanoseconds (blue dots) as well as around 1 minute (red dots). The data points on the same dashed line show the SHG intensity measured from the same flake shortly after (I_t) and 1 min after the THz excitation pulse (I_i), normalized by the SHG signal intensity prior to THz excitation (I_i). Due to the destructive nature of single-shot SHG, I_t , I_i , and I_f were measured at three different spots on the same sample. For this reason, we use #1a, #1b, etc. to emphasize that these data points were taken at different spots (a, b) of

the same flake (#1). The error analysis is provided in Supplementary Note 4. **c** The energy potential as a function of transition coordinate with nonequilibrium carrier distribution (charge neutral). Nonequilibrium distribution of carriers is qualitatively described by the Fermi-smearing method. The free-energy barrier decreases from 1.64 eV to 0.91 eV as the Fermi-smearing width increases from 0.05 eV to 0.5 eV. The figure legend has a unit of eV. **d** The energy potential as a function of transition coordinate upon charge dopings. As the added charge density increases to 1.0 e/MoTe₂, which corresponds to 9×10^{14} cm⁻², the activation energy decreases from 1.66 eV to 1.19 eV. The figure legend has a unit of e/MoTe₂. The atomic structures of transition states are shown in Supplementary Figs. 18 and 19.

relies on the concept of “probe before destruction”^{34,35}, which is well applicable to MoTe₂ (see Supplementary Note 4). The small beam spot for SHG (1 μm) relative to the sample size (≥10 μm) and good spatial uniformity of the trilayer crystals (Supplementary Fig. 11) allow a comparison among three locally destructive single-shot SHG measurements at different sample locations: one prior to THz excitation (I_i), the second at the selected delay time following THz excitation (I_t), and the third at a long delay time at -1 min (I_f).

Figure 3b shows the time evolution of the SHG signal relative to the initial signal following THz excitation (I_t/I_i , blue dots). The response first increases, reaching about twice the initial value at 20 ps. It then remains higher than I_i for several hundred picoseconds, before dropping to $-0.2I_i$ at 12.5 ns. Finally, at long pump-probe delays, the SHG signal disappears completely, indicating the stabilization of a metastable phase. The metastability is further confirmed by the value of the final signals after 1 min of photoexcitation, I_f/I_i , shown as the red dots in Fig. 3b. We were able to reproduce these complex dynamics on different samples, with the initial enhancement of the SHG occurring even below the phase transition threshold (Supplementary Fig. 12). From our single-shot spectroscopy data, we identify a characteristic timescale on the order of 10 ns that is needed to completely switch MoTe₂ out of the 2H polymorph. We attribute the increase in SHG signal observed at shorter times to a possible nucleation of a transient structure with a lower crystalline symmetry than 2H. One such possibility is the distorted trigonal prismatic 2H' phase^{12,14} (Supplementary Fig. 18), which is metastable along the transition pathway and can further prolong the transition timescale. This scenario at short delay times requires additional characterizations by single-shot time-resolved techniques beyond SHG, such as diffraction or visible-IR reflectivity to probe transient lattice and electronic responses, which are beyond the scope of our present study.

Discussion

The set of experimental data from multiple techniques allows us to theoretically explore different effects that can account for the 2H-to-1T' transition. Based on the nanosecond phase transition timescale, a natural hypothesis involves a THz field-driven carrier excitation mechanism. Microscopically, an intense electric field at THz frequency can generate high carrier densities through mechanisms such as Poole-Frenkel ionization, which liberate carriers and accelerate them to multi-eV energies (see Supplementary Note 5). These processes lead to impact ionization, liberating more carriers and evolving as a cascade event³⁶. Such electron-hole generation can lead to either (i) a neutral carrier redistribution when excited carriers remain quasi-free, or (ii) charge doping when carriers localize at the substrate/h-BN interfacial states or spatially separate under the drive of intense THz electric fields especially in the presence of trap states³⁷ (see Supplementary Note 5). To account for both scenarios, we numerically investigated the effects of neutral as well as charged carrier excitation on the energy landscape of MoTe₂.

The results of our calculations are shown in Fig. 3c,d (see Methods and Supplementary Note 6 for details of the first-principles calculations). In equilibrium, the metastable 1T' phase lies about 0.1 eV higher in energy than the 2H phase (blue horizontal lines); here, energy values are quoted per two formula units of MoTe₂ due to unit cell doubling in this transition. The 2H-to-1T' activation barrier and the reverse activation barrier at charge neutrality in equilibrium is 1.66 eV and 1.56 eV, respectively, thus protecting the 2H and 1T' phases against thermal fluctuations. Upon excitation of a neutral electron-hole redistribution (Fig. 3c) or charge doping (Fig. 3d), two effects occur. First, the activation barrier lowers substantially (violet-to-red horizontal lines) and second, the 1T' energy decreases, both effects favoring the occurrence of the 2H-to-1T' transition.

Our joint experimental and theoretical studies establish intense THz fields as a viable route to steer the polymorphic transition in

atomically thin MoTe₂. Crucially, this transition cannot be induced by photons at higher energies^{9–11,38}, as evidenced by our experiments performed with mid-infrared and near-infrared pulses centered around 225 meV and 1.55 eV, respectively (Supplementary Figs. 1 and 2). The key difference between mid- or near-infrared and THz pulses is that the former usually leads to mobile carriers at very high-energy conduction bands, and these high-energy mobile carriers will result in significant lattice heating – hence structural damage including Te cluster formation – through intraband relaxation. On the other hand, strong THz fields can create mobile carriers at the conduction band edge without significant lattice heating effect (see Supplementary Note 5). We also noticed that another mechanism involving THz-excited phonons was proposed to drive the 2H-1T' phase transition in MoTe₂³⁹, which could also contribute to our observation uniquely driven by THz pulses.

The large structural distortion also leads to a significant electronic structure reconstruction involving band inversion around the Γ point, driving a topologically trivial 2H phase of few-layer MoTe₂ into a quantum spin Hall insulator state in the 1T' phase⁴⁰ (see Supplementary Note 7). The capability demonstrated in this work hence opens the tantalizing prospect in the search for phases of matter with non-trivial band topology in addition to highlighting the unique capability of high-field THz pulses in shaping material properties in a complex, multi-phase energy landscape.

Methods

Fabrication of THz field-enhancement structure on fused silica substrate

The fabrication of the metal microslit array was based on a standard photolithography and lift-off process. Image reversal photoresist AZ5214 was spin-coated on a fused silica substrate at 3000 rpm for 30 s, soft baked at 110 °C for 50 s on a hotplate, UV exposed by a maskless aligner MLA 150 with a dose of 24 mJ/cm², and post-exposure baked at 120 °C for 2 min followed by flood exposure and development in AZ422. A thin film of 2-nm Cr was deposited onto the substrate as an adhesion layer by thermal evaporation followed by a 98-nm-thick Au thin film. The sample was soaked in acetone and PG remover for lift-off to complete fabrication of the field enhancement structure.

Layered MoTe₂ integration with the field enhancement structure

The monolayer, few-layer MoTe₂, and layered h-BN were exfoliated on SiO₂/Si substrate from bulk MoTe₂ (HQ graphene) or h-BN crystals. Monolayer and bilayer MoTe₂ were identified by optical contrast and Raman spectroscopy. The layered materials were picked up by a transfer slide composed of a stack of glass, a polydimethylsiloxane (PDMS) film and a polycarbonate (PC) film⁴¹. The resulting stacks of top h-BN layer, MoTe₂ monolayer or bilayer, and bottom h-BN layer were then placed on top of the field enhancement structure with the help of a transfer setup under an optical microscope²⁴. For trilayer or thicker MoTe₂ samples used in the SHG and electron microscopy measurements, h-BN encapsulation was not used.

High-field THz pulse generation

High-field THz pulses were generated in a Mg:LiNbO₃ crystal by tilting the optical pulse front of an 800-nm pump pulse to achieve phase matching⁴². By using a three-parabolic-mirror THz imaging system, the image of the THz beam spot on the sample was focused to its diffraction limit of around 500 μm in diameter. The incident THz pulse temporal profile was measured in the time domain using electro-optic sampling with a 100-μm-thick 110-oriented GaP crystal. When pumping with the 4 W output from an amplified Ti:sapphire laser system (repetition rate 1 kHz, central wavelength 800 nm, pulse duration 100 fs), the peak electric field of the THz pulses reached ~300 kV/cm at the focus, with a spectrum centered at around 0.5 THz (see

Supplementary Figs. 13 and 14). The repetition rate of the laser output was down-counted from 1 kHz to 125 Hz by three successive phase-locked choppers, providing sufficient temporal separation between pulses for a mechanical shutter to isolate single THz pulses.

Spontaneous Raman scattering measurements

Spontaneous Raman scattering was performed on samples before and after THz irradiation using a commercial Raman spectrometer (Horiba LabRAM) with a HeNe laser ($\lambda = 632.8$ nm). The laser beam was focused on the samples by a 100 \times objective into a spot with a diameter of approximately 1 μm .

Transmission electron diffraction microscopy

To prepare the samples for transmission electron microscopy (TEM) characterization before and after THz excitation, we designed a special TEM grid with a THz field enhancement structure. The enhancement pattern made of a 50-nm-thick gold film is deposited on a silicon nitride TEM window. The enhancement structure is a 300- μm -long, 2- μm -wide air gap within the gold film, as shown in Supplementary Fig. 10. We transferred a multilayer MoTe₂ flake on top of the gap using a PDMS dry-transfer method⁴³ and measured the diffraction pattern before and after the single THz pulse excitation. The transmission electron diffraction measurement was performed using a transmission electron microscope (FEI Tecnai Multipurpose Digital TEM) operated at 60 keV at room temperature.

SHG mapping

As shown in Supplementary Fig. 14, the SHG fundamental pulses were provided by a mode-locked Ti:sapphire oscillator centered at 800 nm. The laser pulse duration was around 35 fs at an 80 MHz repetition rate. The pulse was linearly polarized by an achromatic polarizer (400–800 nm) and the polarization at the sample was controlled by an achromatic half-wave plate in a motorized rotational stage. SHG signals from the sample were collected by the same objective for focusing the fundamental light, and they transmitted through the same half-wave plate and polarizer, which ensured that the SHG components detected were parallel to the polarization of the fundamental field. A photomultiplier tube (PMT, Hamamatsu Photonics H10721) was used to analyze the SHG signal. In the fast mapping mode, the laser beam on the sample was scanned using two-axis Galvo mirrors (Thorlabs, GVS412) to acquire in situ SHG images. We also use the SHG mapping method to look for trilayer samples which have uniform response as shown in Supplementary Fig. 11 for the single-shot THz pump-SHG probe measurements.

Single-shot THz pump-SHG probe microscopy

The THz pump arm was combined with SHG pulses from a second, temporally synchronized 12 W amplified Ti:sapphire laser (repetition rate 1 kHz, central wavelength 800 nm, pulse duration 35 fs). SHG light was focused to a near-diffraction-limited size (1 μm) at the sample with a 50 \times objective. The SHG light was collected by the same objective and detected by a PMT with a confocal microscope to selectively probe the area at the focus with single-optical-pulse irradiation. The power level of the SHG excitation pulse was well above the damage threshold of MoTe₂, but the ultrafast nature of the pulse enabled us to obtain a reliable SHG signal before the sample was damaged. The temporal overlap of the counter-propagating THz field and SHG optical pulse was determined by THz field-induced second harmonic signal from a 30- μm -thick LiNbO₃ slab. All of the optical measurements were conducted on a single-shot basis under ambient conditions. More details are given in Supplementary Note 4 and Supplementary Figs. 11d, 15, and 16.

First-principles calculations

We performed density functional theory (DFT) calculations using the VASP code^{44,45} within the general gradient approximation (GGA) –

Perdew-Burke-Ernzerhof (PBE) exchange-correlation functional⁴⁶. The kinetic energy cutoff was 350 eV for the plane-wave basis sets. The lattice constants of 2H and 1T' phases in the neutral state were obtained via structural optimization with a convergence threshold of force on each atom of 0.01 eV/Å, with a vacuum region more than 36-Å-thick to decouple the neighboring slabs. A Γ -centered $11 \times 17 \times 1k$ -point mesh was used to sample the Brillouin zone. The climbing image nudged elastic band (CI-NEB) method⁴⁷ with 5 to 7 intermediate images was used to determine the activation barrier of the phase transition. Besides converging the electronic ground states with charge neutrality, we also considered higher temperature smearing effects and charge doping. More information can be found in Supplementary Note 6 and Supplementary Figs. 17–20.

In these barrier calculations, the in-plane lattice constants were all constrained to the value of the neutral state 2H phase, even for the charged state conditions in which the lattice tends to expand. We note that the treatment of constant area was mainly due to the difficulty of convergence when the lattice vectors were allowed to relax during CI-NEB calculations of charged slabs. It simulates the situation where the lattice of monolayer MoTe₂ is strongly constrained by its interaction with substrates.

Based on the converged electronic ground state with spin-orbit coupling in a given crystal structure, we further constructed the Wannier electronic model using the Wannier90 code^{48,49} by projecting the Mo d-orbitals and Te p-orbitals near the Fermi level. Besides capturing the electronic band structure, the Wannier models also allowed us to investigate the topological properties by evaluating the Z_2 topological index from the non-Abelian Berry connections along the Wilson loop⁵⁰ and the Fu-Kane parity formulation⁵¹ (when inversion symmetry is present). More information can be found in Supplementary Figs. 21–23.

Data availability

Relevant data supporting the key findings of this study are available within the article and the Supplementary Information file. All raw data generated during the current study are available from the corresponding authors upon request.

References

1. Sie, E. J., Nyby, C. M., Pemmaraju, C. D., Park, S. J. & Shen, X. et al. An ultrafast symmetry switch in a Weyl semimetal. *Nature* **565**, 61–66 (2019).
2. Liu, M., Hwang, H. Y., Tao, H., Strikwerda, A. C. & Fan, K. et al. Terahertz-field-induced insulator-to-metal transition in vanadium dioxide metamaterial. *Nature* **487**, 345–348 (2012).
3. Stojchevska, L., Vaskivskiy, I., Mertelj, T., Kusar, P. & Svetin, D. et al. Ultrafast switching to a stable hidden quantum state in an electronic crystal. *Science* **344**, 177–180 (2014).
4. Budden, M., Gebert, T., Buzzi, M., Jotzu, G. & Wang, E. et al. Evidence for metastable photo-induced superconductivity in K₃C₆₀. *Nat. Phys.* **17**, 611–618 (2021).
5. Niziev, V. G. & Nesterov, A. V. Influence of beam polarization on laser cutting efficiency. *J. Phys. D Appl. Phys.* **32**, 1455–1461 (1999).
6. Buchalla, W. & Attin, T. External bleaching therapy with activation by heat, light or laser—a systematic review. *Dent. Mater.* **23**, 586–596 (2007).
7. Popov, V. K., Evseev, A. V., Ivanov, A. L., Roginski, V. V. & Volozhin, A. I. et al. Laser stereolithography and supercritical fluid processing for custom-designed implant fabrication. *J. Mater. Sci.: Mater. Med.* **15**, 123–128 (2004).
8. Zhang, X., Jin, Z., Wang, L., Hachtel, J. A. & Villarreal, E. et al. Low contact barrier in 2H/1T' MoTe₂ in-plane heterostructure synthesized by chemical vapor deposition. *ACS Appl. Mater. Interfaces* **11**, 12777–12785 (2019).

9. Cho, S., Kim, S., Kim, J. H., Zhao, J. & Seok, J. et al. Phase patterning for ohmic homojunction contact in MoTe₂. *Science* **349**, 625–628 (2015).
10. Song, Y., Tian, R., Yang, J., Yin, R. & Zhao, J. et al. Second harmonic generation in atomically thin MoTe₂. *Adv. Opt. Mater.* **6**, 1701334 (2018).
11. Tan, Y., Luo, F., Zhu, M., Xu, X. & Ye, Y. et al. Controllable 2H-to-1T' phase transition in few-layer MoTe₂. *Nanoscale* **10**, 19964–19971 (2018).
12. Kolobov, A. V., Fons, P. & Tominaga, J. Electronic excitation-induced semiconductor-to-metal transition in monolayer MoTe₂. *Phys. Rev. B* **94**, 094114 (2016).
13. Peng, B., Zhang, H., Chen, W., Hou, B. & Qiu, Z.-J. et al. Sub-picosecond photo-induced displacive phase transition in two-dimensional MoTe₂. *npj 2D Mater. Appl.* **4**, 14 (2020).
14. Zhang, F., Zhang, H., Krylyuk, S., Milligan, C. A. & Zhu, Y. et al. Electric-field induced structural transition in vertical MoTe₂- and Mo_{1-x}W_xTe₂-based resistive memories. *Nat. Mater.* **18**, 55–61 (2019).
15. Qi, Y., Naumov, P. G., Ali, M. N., Rajamathi, C. R. & Schnelle, W. et al. Superconductivity in Weyl semimetal candidate MoTe₂. *Nat. Commun.* **7**, 11038 (2016).
16. Wang, Y., Xiao, J., Zhu, H., Li, Y. & Alsaied, Y. et al. Structural phase transition in monolayer MoTe₂ driven by electrostatic doping. *Nature* **550**, 487–491 (2017).
17. Wang, Y., Xiao, J., Chung, T.-F., Nie, Z. & Yang, S. et al. Direct electrical modulation of second-order optical susceptibility via phase transitions. *Nat. Electron.* **4**, 725–730 (2021).
18. Hou, W., Azizimanesh, A., Sewaket, A., Peña, T. & Watson, C. et al. Strain-based room-temperature non-volatile MoTe₂ ferroelectric phase change transistor. *Nat. Nanotechnol.* **14**, 668–673 (2019).
19. Chen, S.-Y., Naylor, C. H., Goldstein, T., Johnson, A. T. C. & Yan, J. Intrinsic phonon bands in high-quality monolayer T' molybdenum ditelluride. *ACS Nano* **11**, 814–820 (2017).
20. Manjón, F. J., Gallego-Parra, S., Rodríguez-Hernández, P., Muñoz, A. & Drasar, C. et al. Anomalous Raman modes in tellurides. *J. Mater. Chem. C* **9**, 6277–6289 (2021).
21. Duerloo, K.-A. N., Li, Y. & Reed, E. J. Structural phase transitions in two-dimensional Mo- and W-dichalcogenide monolayers. *Nat. Commun.* **5**, 1–9 (2014).
22. Keum, D. H., Cho, S., Kim, J. H., Choe, D.-H. & Sung, H.-J. et al. Bandgap opening in few-layered monoclinic MoTe₂. *Nat. Phys.* **11**, 482–486 (2015).
23. Wang, J., Luo, X., Li, S., Verzhbitskiy, I. & Zhao, W. et al. Determination of crystal axes in semimetallic T'-MoTe₂ by polarized Raman spectroscopy. *Adv. Funct. Mater.* **27**, 1604799 (2017).
24. Dean, C. R., Young, A. F., Meric, I., Lee, C. & Wang, L. et al. Boron nitride substrates for high-quality graphene electronics. *Nat. Nanotechnol.* **5**, 722–726 (2010).
25. Wang, L., Meric, I., Huang, P. Y., Gao, Q. & Gao, Y. et al. One-dimensional electrical contact to a two-dimensional material. *Science* **342**, 614–617 (2013).
26. Pein, B. C., Chang, W., Hwang, H. Y., Scherer, J. & Coropceanu, I. et al. Terahertz-driven luminescence and colossal Stark effect in CdSe-CdS colloidal quantum dots. *Nano Lett.* **17**, 5375–5380 (2017).
27. Yamamoto, M., Wang, S. T., Ni, M., Lin, Y.-F. & Li, S.-L. et al. Strong enhancement of Raman scattering from a bulk-inactive vibrational mode in few-layer MoTe₂. *ACS Nano* **8**, 3895–3903 (2014).
28. Beams, R., Cañado, L. G., Krylyuk, S., Kalish, I. & Kalanyan, B. et al. Characterization of few-layer 1T' MoTe₂ by polarization-resolved second harmonic generation and Raman scattering. *ACS Nano* **10**, 9626–9636 (2016).
29. Ruppert, C., Aslan, O. B. & Heinz, T. F. Optical properties and band gap of single- and few-layer MoTe₂ crystals. *Nano Lett.* **14**, 6231–6236 (2014).
30. Wang, L., Xu, Z., Wang, W. & Bai, X. Atomic mechanism of dynamic electrochemical lithiation processes of MoS₂ nanosheets. *J. Am. Chem. Soc.* **136**, 6693–6697 (2014).
31. Gao, P., Wang, L., Zhang, Y., Huang, Y. & Liu, K. Atomic-scale probing of the dynamics of sodium transport and intercalation-induced phase transformations in MoS₂. *ACS Nano* **9**, 11296–11301 (2015).
32. Heising, J. & Kanatzidis, M. G. Exfoliated and restacked MoS₂ and WS₂: Ionic or neutral species? Encapsulation and ordering of hard electropositive cations. *J. Am. Chem. Soc.* **121**, 11720–11732 (1999).
33. Meng, L., Ma, Y., Si, K., Xu, S. & Wang, J. et al. Recent advances of phase engineering in group VI transition metal dichalcogenides. *Tungsten* **1**, 46–58 (2019).
34. Chapman, H. N., Fromme, P., Barty, A., White, T. A. & Kirian, R. A. et al. Femtosecond X-ray protein nanocrystallography. *Nature* **470**, 73–77 (2011).
35. Tenboer, J., Basu, S., Zatsepin, N., Pande, K. & Milathianaki, D. et al. Time-resolved serial crystallography captures high-resolution intermediates of photoactive yellow protein. *Science* **346**, 1242–1246 (2014).
36. Fan, K., Hwang, H. Y., Liu, M., Strikwerda, A. C. & Sternbach, A. et al. Nonlinear terahertz metamaterials via field-enhanced carrier dynamics in GaAs. *Phys. Rev. Lett.* **110**, 217404 (2013).
37. Ju, L., Velasco, J., Huang, E., Kahn, S. & Nosioglia, C. et al. Photo-induced doping in heterostructures of graphene and boron nitride. *Nat. Nanotechnol.* **9**, 348–352 (2014).
38. Krishnamoorthy, A., Lin, M.-F., Zhang, X., Weninger, C. & Ma, R. et al. Optical control of non-equilibrium phonon dynamics. *Nano Lett.* **19**, 4981–4989 (2019).
39. Zhou, J., Xu, H., Shi, Y. & Li, J. Terahertz driven reversible topological phase transition of monolayer transition metal dichalcogenides. *Adv. Sci.* **8**, 2003832 (2021).
40. Qian, X., Liu, J., Fu, L. & Li, J. Quantum spin Hall effect in two-dimensional transition metal dichalcogenides. *Science* **346**, 1344–1347 (2014).
41. Zomer, P. J., Guimarães, M. H. D., Brant, J. C., Tombros, N. & van Wees, B. J. Fast pick up technique for high quality heterostructures of bilayer graphene and hexagonal boron nitride. *Appl. Phys. Lett.* **105**, 013101 (2014).
42. Hebling, J., Yeh, K.-L., Hoffmann, M. C., Bartal, B. & Nelson, K. A. Generation of high-power terahertz pulses by tilted-pulse-front excitation and their application possibilities. *J. Opt. Soc. Am. B* **25**, B6–B19 (2008).
43. Bie, Y.-Q., Zong, A., Wang, X., Jarillo-Herrero, P. & Gedik, N. A versatile sample fabrication method for ultrafast electron diffraction. *Ultramicroscopy* **230**, 113389 (2021).
44. Kresse, G. & Furthmüller, J. Efficient iterative schemes for ab initio total-energy calculations using a plane-wave basis set. *Phys. Rev. B* **54**, 11169–11186 (1996).
45. Kresse, G. & Furthmüller, J. Efficiency of ab-initio total energy calculations for metals and semiconductors using a plane-wave basis set. *Comput. Mater. Sci.* **6**, 15–50 (1996).
46. Perdew, J. P., Burke, K. & Ernzerhof, M. Generalized gradient approximation made simple. *Phys. Rev. Lett.* **77**, 3865–3868 (1996).
47. Henkelman, G., Uberuaga, B. P. & Jónsson, H. A climbing image nudged elastic band method for finding saddle points and minimum energy paths. *J. Chem. Phys.* **113**, 9901–9904 (2000).
48. Mostofi, A. A., Yates, J. R., Lee, Y.-S., Souza, I. & Vanderbilt, D. et al. wannier90: a tool for obtaining maximally-localised Wannier functions. *Comput. Phys. Commun.* **178**, 685–699 (2008).
49. Mostofi, A. A., Yates, J. R., Pizzi, G., Lee, Y.-S. & Souza, I. et al. An updated version of wannier90: a tool for obtaining maximally-localised Wannier functions. *Comput. Phys. Commun.* **185**, 2309–2310 (2014).

50. Yu, R., Qi, X. L., Bernevig, A., Fang, Z. & Dai, X. Equivalent expression of \mathbb{Z}_2 topological invariant for band insulators using the non-Abelian Berry connection. *Phys. Rev. B* **84**, 075119 (2011).
51. Fu, L. & Kane, C. L. Topological insulators with inversion symmetry. *Phys. Rev. B* **76**, 045302 (2007).

Acknowledgements

The authors acknowledge discussions and technical supports from Z.F. Ren, X. Wang, A. Sood, Y. Yoon, B. Pein, P.-C. Shen, A. Maznev, T. Mahony, F. Gao, and Y. Chen. J.S. and K.A.N. acknowledge support from the U.S. Department of Energy, Office of Basic Energy Sciences, under Award No. DE-SC0019126. P.J.-H. acknowledges support from Gordon and Betty Moore Foundation's EPiQS Initiative through grant GBMF4693. A.Z. acknowledges support from the Miller Institute for Basic Research in Science. W.C., S.F. and E.K. acknowledge support by ARO MURI award W911NF-14-0247. S.F. is also supported by a Rutgers Center for Material Theory Distinguished Postdoctoral Fellowship. J.-C.H. and V.B. acknowledge support from the Center for Energy Efficient Electronics Science (NSF Award 0939514). Y.-Q.B. and Z.C.L. acknowledges support from National Natural Science Foundation of China (Grant No.'s 61974167 and 91963205), the National Key R&D Program of China (No. 2019YFA0210203) and No. 2019QN01X113. Y.-Q.B. further acknowledges the Open Project of Guangdong Province Key Lab of Display Material and Technology (No. 2020B1212060030). K.W. and T.T. acknowledge support from the Elemental Strategy Initiative conducted by the MEXT, Japan (Grant No. JPMXP0112101001) and JSPS KAKENHI (Grant No.'s 19H05790 and JP20H00354). E.B. was supported by the ARL-UT Austin Cooperative Agreement W911NF-21-2-0185. X.F. acknowledges support from National Natural Science Foundation of China (Grant No.'s 11974191 and 2217830).

Author contributions

Y.-Q.B., J.S. and A.Z. conceived the experiments, performed the measurements, and analyzed the data. W.C., S.F. and E.K. provided theoretical calculations. Y.-Q.B., J.H., and V.B. fabricated field enhancement structures. Y.Z. helped with the electron diffraction measurements. Y.-Q.B. and X.F. performed energy-dispersive X-ray spectroscopy. Z.C. performed the field enhancement calculations. T.T. and K.W. grew the crystals of hexagonal boron nitride. A.Z., Y.-Q.B., J.S. and E.B. led the

manuscript preparation with input from all authors. The project was supervised by Y.-Q.B., P.J.-H. and K.A.N.

Competing interests

The authors declare no competing interests.

Additional information

Supplementary information The online version contains supplementary material available at <https://doi.org/10.1038/s41467-023-41291-w>.

Correspondence and requests for materials should be addressed to Ya-Qing Bie, Pablo Jarillo-Herrero or Keith A. Nelson.

Peer review information *Nature Communications* thanks Burak Guzel-turk and the other, anonymous, reviewer(s) for their contribution to the peer review of this work.

Reprints and permissions information is available at <http://www.nature.com/reprints>

Publisher's note Springer Nature remains neutral with regard to jurisdictional claims in published maps and institutional affiliations.

Open Access This article is licensed under a Creative Commons Attribution 4.0 International License, which permits use, sharing, adaptation, distribution and reproduction in any medium or format, as long as you give appropriate credit to the original author(s) and the source, provide a link to the Creative Commons license, and indicate if changes were made. The images or other third party material in this article are included in the article's Creative Commons license, unless indicated otherwise in a credit line to the material. If material is not included in the article's Creative Commons license and your intended use is not permitted by statutory regulation or exceeds the permitted use, you will need to obtain permission directly from the copyright holder. To view a copy of this license, visit <http://creativecommons.org/licenses/by/4.0/>.

© The Author(s) 2023